JOURNAL OF GUIDANCE, CONTROL, AND DYNAMICS
Vol. 42, No. 5, May 2019

Engineering Notes

Simulated Formation Flight of Nanosatellites Using Differential Drag with High-Fidelity Rarefied Aerodynamics

Daniel S. Groesbeck,* Kenneth A. Hart,* and Brian C. Gunter†
Georgia Institute of Technology, Atlanta, Georgia 30332-0150

DOI: 10.2514/1.G003871

Nomenclature

A	=	cross-sectional area, cm^2
a	=	acceleration rate, m/s^2
C	=	coefficient; see subscripts

Subscripts

M	=	mass of the spacecraft, kg
$\dot{Q}$	=	total convective heat rate, mW
r_0	=	radial basis function tuning parameter
t_D	=	time to delay maneuver, s
t_M	=	length of time for maneuver, s
V_M	=	separation velocity between satellites, m/s
$\hat{V}_\infty$	=	freestream velocity direction
ρ	=	atmospheric density, kg/m^3
σ	=	accommodation coefficient

Subscripts

A	=	axial
D	=	drag
N	=	normal
S	=	side
T	=	tangential

I. Introduction

THE control and utilization of small-satellite constellations and formations are particularly challenging due to the resource constraints involved for nanosatellites. One example of this is the Ranging and Nanosatellite Guidance Experiment (RANGE) mission [1]. This two-satellite CubeSat mission consists of two 1.5U (1U = 10 × 10 × 10 cm) satellites in a leader–follower formation (see Fig. 1), with the goal of improving the absolute and relative positioning capabilities of CubeSats. The satellites have no onboard propulsion system, and they will rely on differential drag techniques to control their relative position. Each satellite will receive Global Positioning System (GPS) telemetry data and will communicate with the Georgia Tech (GT) ground station via Ultra High Frequency (UHF) transmitters.

Differential drag is the concept of using changes in satellite orientation to create different drag profiles. This process was originally proposed by Leonard, Hollister, and Bergmann in 1989 for formation keeping [2]. When one satellite changes its attitude, the drag force increases or decreases, and the satellite changes its kinetic energy. Although intuition might suggest that an increase in drag force would slow the satellite's velocity, in reality, the increase in this force causes the satellite to drop in altitude. Although this may cause a short-term lag, the drop in altitude reduces the satellites orbital period and, in turn, actually increases the satellite's relative velocity.

With the increased usage of CubeSats, which typically do not have onboard propellant, this concept has gained renewed interest. Horsley et al. theorized that lift could be generated using differential drag and could be used for satellite rendezvous [3,4]. Meanwhile, The Aerospace Corporation experimented with differential drag as part of their Aerocube-4 mission [5]. Omar and Wersinger looked further at various atmospheric models to evaluate differential drag maneuver times in 2015 [6].

There is also significant research being performed in the area of controller design for satellites using differential drag. In 2016, Peŕez and Bevilacqua evaluated using a Lyapunov controller with predictive atmospheric density for differential drag control between satellites [7]. Additionally, Mazal et al. wrote about including bounded uncertainties into the control laws of satellites using differential drag for rendezvous [8]. Planet (formerly Planet Labs) has likewise been doing extensive research on differential drag with their CubeSats, specifically with regard to a ground-based controller to distribute satellites globally [9–11].

The RANGE mission will provide new insights into this topic by 1) demonstrating close-range formation keeping using only differential drag, and 2) exploring high-fidelity mission operation scenarios using rarefied flow drag modeling. This Note describes the underlying methodologies behind these contributions, which will be validated and refined after the RANGE satellites launch. The successful implementation of the methods described in this study would represent a significant advance in the overall design and control of small-satellite formations and constellations in low Earth orbit.

In Sec. II, this Note discusses the development of the rarefied flow model, using surrogate modeling, and the validation process of this model. Additionally, in Sec. III, comparisons are made between satellites with and without rarefied flow dynamics used in conjunction with a high-precision orbit propagation (HPOP) tool. Finally, Sec. IV is a case study of the initial maneuvers of the RANGE CubeSat mission. The satellites have a separation kickoff force applied to them, and mission planning using differential drag is evaluated.

II. Rarefied Flow

To accurately predict the relative motion of the RANGE spacecraft caused by atmospheric drag requires detailed knowledge of the atmospheric environment and its interaction with the surface of the satellites. The simplest approach, adopted by nearly all small-satellite missions, is to use a simple drag force expression that is proportional to the alongtrack drag area/velocity, atmospheric density, and a spacecraft drag coefficient [12]. These methods do not account for the true rarefied flow environment of space. One of the objectives of this study is to evaluate whether incorporation of rarefied flow in the drag modeling is significant when predicting the relative motion of the satellites due to drag.

Received 6 June 2018; revision received 21 October 2018; accepted for publication 27 October 2018; published online 31 December 2018.

*Graduate Student, Daniel Guggenheim School of Aerospace Engineering. Student Member AIAA.

†Assistant Professor, Daniel Guggenheim School of Aerospace Engineering. Senior Member AIAA.

The direct simulation Monte Carlo (DSMC) approach to computational fluid dynamics removes the continuum assumption on the fluid and applies gas kinetic theory [13]. The order of magnitude of the problem is reduced through simulated particles but, otherwise, the mechanics of collisions, rotation, and thermal motion are included. This study uses an industry standard code developed at NASA called the DSMC analysis code (DAC).

Calling the DAC for each time step of an orbit propagation would be computationally inefficient because there are many time steps and small changes in attitude between time steps. Instead, a design of experiments is used to run the DAC before the orbit propagation; then, these results are queried using a surrogate model. Training and validation points for the model were selected using an iterative space-filling design.

A. Geometry Model

The geometry of the RANGE satellite is shown in Fig. 2. The z axis of the satellite is nadir pointing. These axes are fixed to the satellite, and the aerodynamics are calculated with respect to these axes. The axial force coefficient C_A corresponds with the x axis, the side force coefficient C_S corresponds with the y axis, and the normal force coefficient C_N corresponds with the z axis.

B. Relevant Properties

The properties of the low-Earth-orbit (LEO) atmosphere are sensitive to several factors, including altitude, latitude, time of day, time of year, and solar activity. Table 1 provides the values of these properties that were used in developing the RANGE aerodynamic model [14,15]. In the NRLMSISE atmospheric model [16], the values of latitude and longitude are set to zero and the date is late 2017, which is near solar minimum.

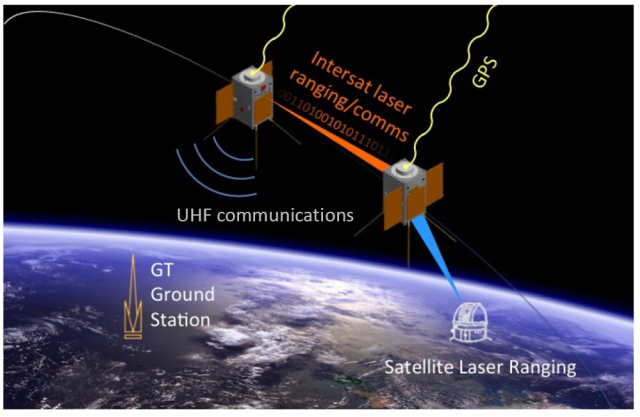

Fig. 1 RANGE mission operational view.

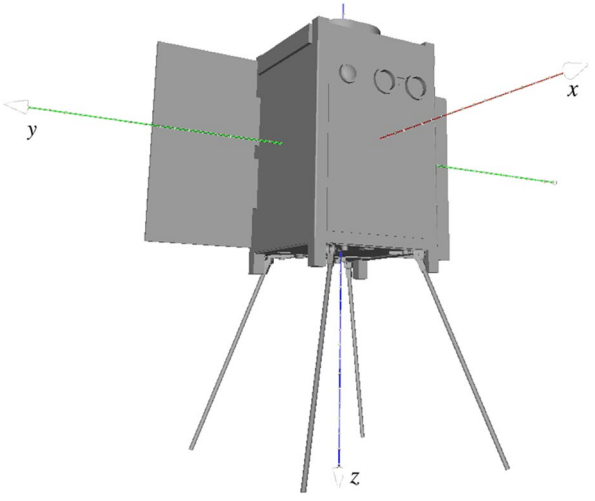

Fig. 2 Computer image of a RANGE satellite: x is intrack, y is cross track, and z is nadir pointing.

Table 1 Model values of relevant properties

Property	Symbol	Value	Unit	Source
		Orbit		
Altitude	h	450	km	Assumed
Speed	V_∞	7.65	km/s	Assumed circular
		Satellite		
Reference length	l_{ref}	10	cm	— —
Reference area	A_{ref}	450	cm^2	— —
Surface temperature	T_W	300	K	Assumed
		Atmosphere		
Density	ρ_∞	1.28×10^{-12}	kg/m^3	Ref. [14]
Temperature	T_∞	943	K	Ref. [14]
Composition (molar)	χ_{O}	0.92	— —	Ref. [14]
	χ_{He}	0.05	— —	Ref. [14]
	χ_{N_2}	0.03	— —	Ref. [14]
Mean free path	λ	63	km	Ref. [15]
Mach number	M	12	— —	Ref. [15]
Knudsen number	Kn	6.3×10^8	— —	$Kn = \lambda/l_{\text{ref}}$
Molecular speed ratio	s	10.2	— —	$s = V_\infty/\sqrt{2RT_\infty}$
		Gas–surface interaction		
Accommodation coefficient	σ	0.86	— —	See Sec. II.C

The accommodation coefficient cannot be observed reliably before flight; there will be uncertainty in the aerodynamic force and moment coefficients of the RANGE nanosatellites. The accommodation coefficient for the Ariel 2 mission, which had a perigee altitude of 290 km and an eccentricity of 0.07, was calculated to be 0.86 [17,18]. Accommodation coefficients for satellites in the 800–1000 km range have been studied; however, at this altitude, the abundance of helium is dominant over atomic oxygen [19]. Because the atmosphere that the nanosatellites will fly through is most similar to the atmosphere experienced by Ariel 2, an accommodation coefficient of 0.86 is assumed for the RANGE. Compared to full accommodation, which is common at lower altitudes, the aerodynamics are approximately 5% different; therefore, that the overall uncertainty in the numerical results is 5%. This relative error was determined by recalculating the aerodynamic coefficients with an accommodation coefficient of 1.00, for 120 orientations, and comparing the magnitude of the error in the aerodynamic force vector with the magnitude of the force vector.

C. Free Molecular Flow Theory

This flow is classified as a free molecular based on the Mach number and Knudsen number [20]. Additionally, the high molecular speed ratio s [Eq. (1)] indicates that the flow is hyperthermal [21]. The pressure and shear coefficients, C_p and C_T, in hyperthermal free molecular flow are given in Eqs. (2) and (3), where $\sigma_{N,T}$ are the accommodation coefficients, θ is the angle of incidence, and $T_{W,\infty}$ are the temperatures of the wall and freestream, respectively. Given that the molecular speed ratio is 10.2, the hyperthermal limit applies as shown in Eqs. (4) and (5). As can be seen, the surface temperature and gas temperature do not significantly contribute to the aerodynamics. In these flow conditions, the aerodynamics depend strongly on the accommodation coefficient and angle of incidence:

$$s = \frac{V_\infty}{\sqrt{2RT_\infty}} \tag{1}$$

$$C_p = \frac{1}{s^2}\left[\left(\frac{2-\sigma_N}{\sqrt{\pi}} s\sin(\theta) + \frac{\sigma_N}{2}\sqrt{\frac{T_w}{T_\infty}}\right)e^{-(s\sin\theta)^2} + \left\{(2-\sigma_N)\left((s\sin\theta)^2 + \frac{1}{2}\right) + \frac{\sigma_N}{2}\sqrt{\frac{\pi T_w}{T_\infty}} s\sin\theta\right\}(1+\text{erf}(s\sin\theta))\right] \tag{2}$$

$$C_\tau = \frac{\sigma_T \cos\theta}{s\sqrt{\pi}}\left[e^{-(s\sin\theta)^2} + \sqrt{\pi}s\sin\theta(1+\operatorname{erf}(s\sin\theta))\right] \quad (3)$$

$$\lim_{s\to\infty} C_p = 2(2-\sigma_N)\sin^2\theta \quad (4)$$

$$\lim_{s\to\infty} C_\tau = 2\sigma_T \sin\theta\cos\theta \quad (5)$$

Accommodation coefficients describe the average distribution of reflected velocities. Measuring these quantities independently is possible under controlled conditions, although laboratory experiments and flight data vary significantly [17,22]. Flight data assume that σ_N and σ_T are equal, and the symbol σ is used instead. This is equivalent to Maxwell's description of free molecular flow, where σ represents the fraction of molecular collisions that are diffuse [23].

The DSMC approach is applied to this flow, instead of a free molecular code, because of the satellite geometry. Flow striking the solar panels could reflect onto the satellite and collide multiple times, and so the DSMC is used to model the flow instead. In the DSMC, molecules are grouped together into simulated particles to decrease computational cost but, otherwise, the fundamental conservation laws of mass, momentum, and energy are preserved [13]. NASA has developed a DAC that provides the forces, moments, and aerodynamic heating in a two-step process with mesh adaptation [24]. The DAC tool is used to generate the aerodynamic database for the RANGE nanosatellites.

D. Surrogate Modeling

The aerodynamic coefficients produced by the DAC are specific to a single freestream orientation. The DAC can be run multiple times to generate a table of discrete orientations and coefficients. For orientations that are not exactly identical to those samples, an interpolation model is needed to predict the coefficient values. In this section, a surrogate model and an interpolation model are used interchangeably because the model uses radial basis functions (RBFs), and RBFs interpolate through the training data. The RBF model is used instead of a nearest-neighbor lookup or a linear interpolation model because those methods have greater modeling errors for the same amount of training data as compared to a RBF.

The interpolation model requires training data from a grid of orientations. It was unknown a priori how fine the grid would need to be, and so an iterative grid technique was developed. A total of five iterations on the grid were run, representing 1026 DAC runs. Initially, a model was trained on the runs from iteration 1 and validated against the results from iterations 2–5. That model had up to a 50% error, and so the runs from iteration 2 were added to the training data and removed from the validation data. This process continued until the errors were below 5% because that was the uncertainty in the aerodynamic coefficients. The final model was trained on the results from $N = 1, 2, 3$, and 4, and then it was validated against the results from $N = 5$.

The final step in generating this model is choosing the RBF tuning parameter r_0. This parameter is chosen by minimizing the error between the model predictions and validation data.

1. *Design of Experiments*

The space of all possible orientations of the flowfield $\hat{V}_\infty$ is a unit sphere $\mathbb{S}^2$. Baumgardner and Frederickson developed an icosahedral discretization of the sphere, which began with an icosahedron, bisected the edges with new vertices, projected these vertices onto the unit sphere, and then created new faces from these vertices and repeated [25]. One advantage to this bisection method was that the grid was nearly uniform across the unit sphere. The design of experiments used in this investigation starts instead with an octahedron and uses the same bisection and iteration process. Projection is not used in this process. Instead, in the bisection step, the unit vector of one vertex is rotated through half the angle to the joining vertex. This change simplifies the process by eliminating the need for polyhedron-to-sphere conversion.

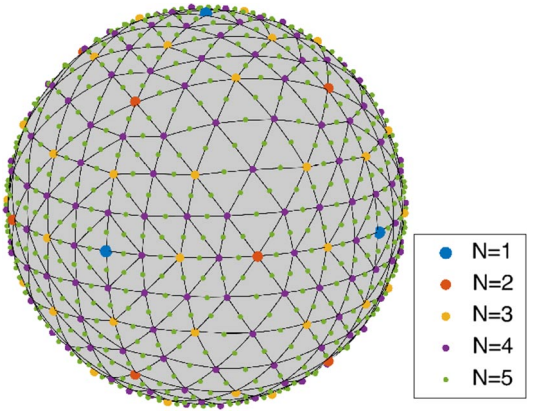

Fig. 3 Sample points for iterative octahedral design of experiments.

The designs of experiments are shown in Fig. 3. The $N = 2$ points each bisect the lines between the $N = 1$ points. The $N = 3$ points bisect the $N = 1$ points and $N = 2$ points. The process can be repeated ad infinitum; however, the number of sample points grows rapidly. The growth rate for the number of vertices V is derived from the Euler characteristic and given in Eq. (6):

$$V(N) = 2 + 4^N \quad (6)$$

2. *Grid Convergence*

Shown in Fig. 4 is a comparison of the distributions of errors based on the number of iterations on the octahedron. The model is trained with the points from $N \le n$ and compared against the results from $N > n$. The octahedral design of experiments is accurate up to 50%, whereas the next iteration is good to within 20%, and the following iteration is good to within 8%. The fourth iteration, $N = 4$ in Figs. 3 and 4, is accurate to within 3.5% of the values from $N = 5$, and so the grid converges to within 5% at $N = 4$.

At the fourth iteration ($N = 4$), the maximum relative error in the model was 3.5% when compared against the $N = 5$ results. Because the target accuracy was 5%, the grid converged at $N = 4$.

3. *Interpolation Function*

There are four common interpolation techniques for data distributed on a sphere: linear interpolation, RBFs, cubic interpolation, and spherical harmonics. The RBF approach is used in this investigation because it can be tuned to maximize the fit and does not rely on gradient approximations. Two RBF kernels are used in the meteorological community; thin-plate spline and multiquadric are both very sensitive to the value of their parameter r_0 [26].

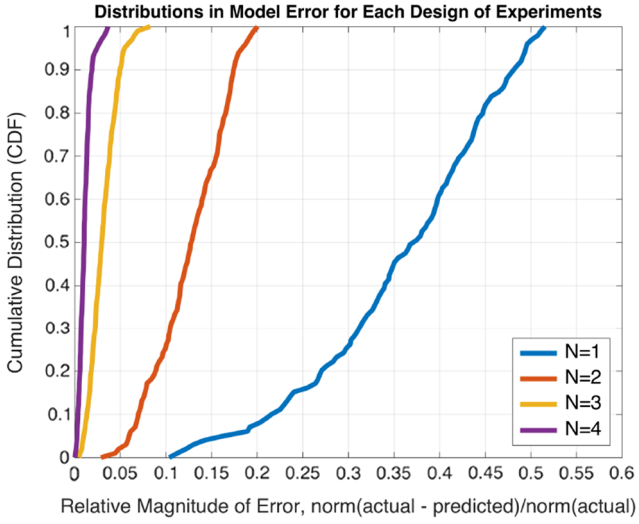

Fig. 4 Error distributions for each design of experiments.

After creating interpolation functions using both kernels, it is discovered that the inverse multiquadric RBF kernel, given in Eq. (8), is relatively insensitive to r_0 and generally yields lower errors. In this application of RBFs, the distance r is the angle between the points on the sphere. The construction of the interpolation function is given in Eqs. (7–10), in which there are n unit vectors $\hat{u}_i$. RBF kernels are used in the meteorological community; thin-plate spline and multiquadric are both very sensitive to the value of their parameter r_0 [26]. The inverse multiquadric RBF kernel, given in Eq. (8), is relatively insensitive to r_0 and generally yields lower errors. In this application of RBFs, the distance r is the angle between the points on the sphere. The construction of the interpolation function is given in Eqs. (7–10), in which there are n unit vectors $\hat{u}_i$:

$$\boldsymbol{f}(\hat{V}_\infty) \approx \hat{\boldsymbol{f}}(\hat{V}_\infty) = \sum_{i=1}^{n} \phi(\cos^{-1}(\hat{V}_\infty \cdot \hat{u}_i))\boldsymbol{w}_i \tag{7}$$

$$\phi(r) = \frac{1}{\sqrt{r^2 + r_0^2}} \tag{8}$$

$$\Phi_{ij} = \phi(\cos^{-1}(\hat{u}_i \cdot \hat{u}_j)) \quad \forall\ i, j = 1, \ldots, n \tag{9}$$

$$\boldsymbol{w}_i = \sum_{j=1}^{n} \Phi_{ij}^{-1} \boldsymbol{f}(\hat{u}) \tag{10}$$

The training points for the RBF interpolant are a subset of all the sample points. Specifically, the training points are the vertices $\hat{u}_j$ of the spherical triangle containing the query point $\hat{V}_\infty$. Which triangle contains the query point is determined by checking that the point is to the left of every edge, in a counterclockwise sense. Downselecting to three training points improves the model fit error (MFE) of the interpolant and decreases the computational cost for inverting the matrix Φ.

4. *RBF Parameter Tuning*

The parameter of the RBF r_0 can be tuned to improve the MFE of the interpolant. Selecting the value for r_0 is the result of the optimization problem stated in Eq. (11). In this set of equations, there are m validation points. The objective function is the sum of the sample mean squared and the sample variance. The samples are the 2-norm of the difference in the validation outputs and the predicted outputs. These outputs are the three force components, the three moment components, and the aerodynamic heating, each in metric base units. Because the moments and heat rates are small, this residual is equivalent to the magnitude of the error in the force only:

$$\begin{aligned} \min_{r_0} \quad & \bar{x}^2 + s^2 \\ \text{subject to} \quad & x_j = \|\boldsymbol{f}_j - \hat{\boldsymbol{f}}_j\|_2 \\ & \bar{x} = \sum_{j=1}^{m} x_j \\ & s^2 = \frac{1}{m-1} \sum_{j=1}^{m} (x_j - \bar{x})^2 \\ & 0 \le r_0 \end{aligned} \tag{11}$$

The constraints in Eq. (11) are definitions for the samples, mean, and variance; and they are not truly equality constraints on r_0. This is a single-objective single-variable optimization problem with one side constraint because ϕ is symmetric in r_0. This problem is solved by first bounding the minimum, and then applying the golden section method [27]. The minimizing value of r_0 depends on the number of training points, which is determined by the number N performed in the design of experiments. Table 2 is the values for r_0 from $N = 1$ to 4.

Table 2 Tuned values of r_0

N	r_0
1	1.33
2	0.91
3	0.89
4	0.96

E. Validation

The DSMC simulation results become self-consistent after $N = 4$ iterations. Analytic models provide a basis of comparison for the simulation results because the two have produced results within a 10–15% difference in previous investigations [28]. In these cases, the DSMC is more accurate because analytic models are based on several assumptions of the flow and the geometry. An analytic model of the aerodynamics was developed for validation using the hyperthermal pressure and shear coefficients and the superposition methodology [28]. The outputs from the DAC are compared against this model in Figs. 5 and 6. There is good agreement between the DAC outputs and the analytic model in the aerodynamic force coefficients. The analytic model does not capture the effects of self-reflection, and so there are small deviations in these results. The moment coefficients C_m and C_n are greatly overstated in the analytic model; flat plates near the center of reference should generate very little moment. Overall, the DSMC simulation results and analytic results are on the right scale and show similar trends.

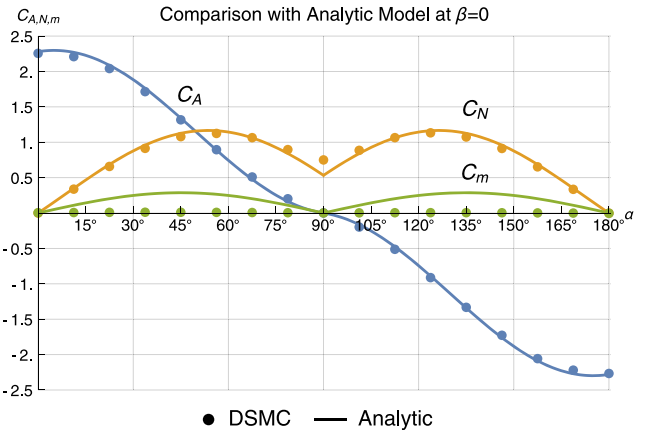

Fig. 5 Comparison of DAC output with analytic model: sweeping angle of attack.

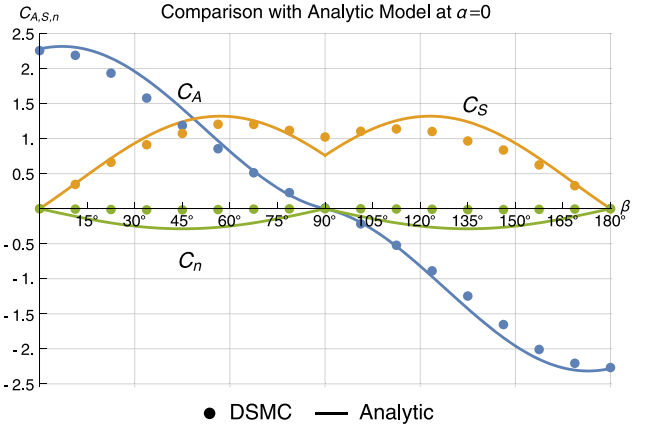

Fig. 6 Comparison of DAC output with analytic model: sweeping sideslip angle.

Table 3 Drag coefficients for flow oriented along coordinate axes

Axis	C_D
$+x$	2.27
$+y$	1.03
$+z$	0.75
$-x$	2.26
$-y$	1.02
$-z$	0.75

F. Discussion of Results

1. *Drag Along the Body Axes*

Because the high- and low-drag modes are along the coordinate axes of the satellite, the drag coefficients in axis-aligned configurations are most important and are given in Table 3. The full aerodynamic database is provided in the supplemental material and contains the body-fixed aerodynamic coefficients, the wind-frame coefficients, and the convective heating rate. The lift coefficient is the total force coefficient perpendicular to the freestream.

2. *Aerodynamic Moments*

The moments imparted onto the satellite are relatively small in magnitude as compared to the forces; however, the moments are also scaled by the reference length. The order of magnitude of the freestream dynamic pressure is 10 μPa, and the moment coefficients (multiplied by the reference area and reference length) are on the order of 100 cm^3. The magnitude of the moments will be on the order of 1 nN $\cdot$ m, which is significantly smaller than the other torques acting on the satellite.

3. *Aerodynamic Heating*

In addition to the forces and moments on the satellite, the DAC calculates the convective heating on the satellite $\dot{Q}$. The heat flux distribution could be calculated in the DAC postprocessing; however, the surface-integrated quantity is sufficiently small. The convective $\dot{Q}$ values are between 5 and 14 mW, which correspond to the minimum and maximum projected areas.

4. *Comparison with Sphere and Plate Models*

The analytic geometry used in Sec. II.E included the multiple facets and shadowing conditions specific to the RANGE nanosatellite. Simpler analytic models (the flat plate and sphere models) are typically included in trajectory propagation tools. These models are shown against the DAC data in Figs. 7 and 8. Neither of these models captures the trends in the aerodynamics of the RANGE nanosatellite. Using the drag coefficient as a figure of merit, the sphere and plate models differ from the DAC results by 102 and 65%, respectively, and at the 80% confidence level.

III. Differential Drag

To prepare for mission operations, a high-precision orbit propagation plug-in for Analytic Graphics, Inc.'s Systems Tool Kit[‡] was developed to account for rarefied flow characteristics and a maneuver control system. By changing the attitude of the satellites into various drag profiles, different ballistic coefficients are created. Adjustments in orientation lead to changes in the separation distance of the two satellites over a short time interval. When these satellites are in LEO, the potential drag is small, but it accumulates over time. This drag effect can be useful for small satellites at low altitudes, such as the RANGE satellites, because it enables mission planning maneuvers without an onboard propellant system. By making changes in the orientations of the two satellites, the linear distance between them can either be increased or decreased.

[‡]Data available online at https://www.agi.com/products/stk [retrieved 2018].

The plug-in uses the rarefied aerodynamics database for the RANGE satellites discussed in Sec. II to calculate the expected forces that each RANGE satellite would experience in any orientation. The standard HPOP propagator uses user-supplied constants of mass M, cross-sectional area A, and a drag coefficient C_D to calculate the ballistic coefficient (BC) described in Eq. (12):

$$\mathrm{BC} = \frac{M}{C_D A} \tag{12}$$

The difficulty with this model is that the cross-sectional area and the drag coefficient will, in reality, be constantly fluctuating. This plug-in allows the propagator to have variable inputs based on the attitude of a satellite. This is an accurate way to predict the behavior of a small satellite without onboard propulsion that will be performing maneuvers by just shifting orientation.

Model comparison was done analyzing the results of the propagator with the plug-in against data generated using a constant ballistic coefficient. These results were then used to estimate various differential drag scenarios for the RANGE mission and the corresponding maneuvers required to increase or decrease the satellite's relative distance. Further detail on the development of the propagator and comparisons to previous missions by the Aerospace Corporation and Planet can be found in the work of Groesbeck et al. [29].

A. RANGE Satellite Model Comparison Analysis

A model comparison contrasting the results of the plug-in against the outputs of the same satellites using only the HPOP propagator with no plug-in and constant C_D, A, and M values was performed. This was done to observe the magnitude of the difference in position,

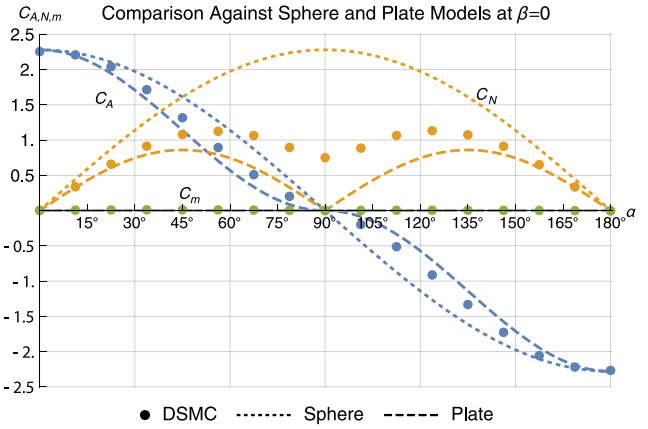

Fig. 7 Comparison of DAC output with sphere and plate models: sweeping angle of attack.

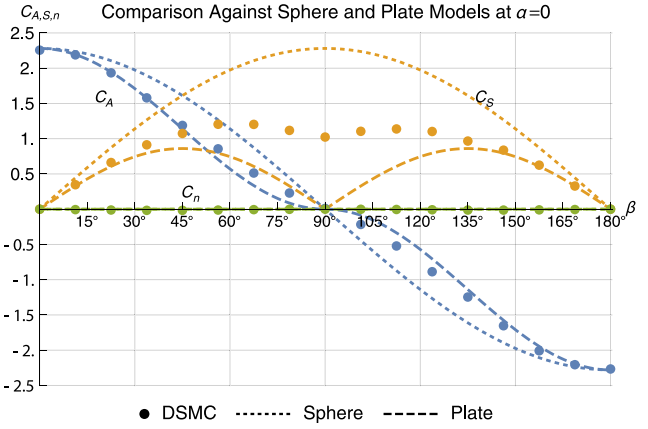

Fig. 8 Comparison of DAC output with sphere and plate model: sweeping sideslip angle.

drag, and drift rates that would be viewed between the predictive model using rarefied flow characteristics and the standard HPOP model. To perform the model comparison analysis, two RANGE satellites were put into a scenario with identical orbital elements. One satellite was placed in the high-drag mode and one was placed in the low-drag mode. The high-drag mode had the satellite antennas nadir pointing and the largest surface area pointing toward the freestream velocity, whereas the low-drag mode had the smallest surface area toward the freestream velocity. These satellites were propagated using the plug-in that had been created. A second set of satellites was added that would have all the exact same characteristics of the first two satellites, but these two would operate without the plug-in.

Although it was necessary to see how far the satellites separated depending on the type of model used, it was more valuable to evaluate the separation distance between the high- and low-drag satellites when comparing models. Figure 9 shows the linear separation distance between the high- and low-drag satellites over a 48 h period using the different models. Although the two plots appear to be very similar, the difference between the two models grows to over 800 m by the end of the simulation period, as observed in Fig. 10. This means that a low-fidelity drag model can create significantly different trajectories in a matter of hours of simulation time.

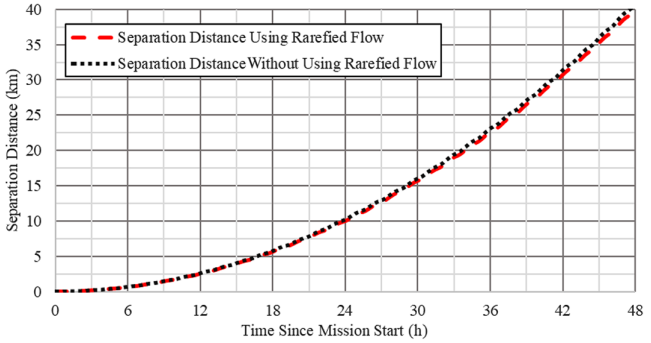

Fig. 9 Linear distance between satellites for models with and without the plug-in.

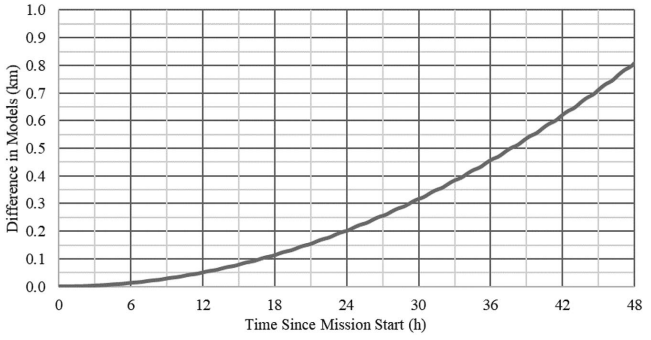

Fig. 10 Difference in distance between the models with and without the plug-in.

B. RANGE Maneuver Analysis

To analyze different maneuvers, various orientations were input into the plug-in code to find the separation rates under initial conditions. The increase in linear separation distance is solely due to the difference in orientation. The reference orientation is the high-drag mode, in which the satellite x axis is pointed intrack and the z axis is pointed nadir. The attitudes considered in this study are rotations about the satellite y axis.

To test for acceleration rates, one satellite was in a fixed high-drag mode orientation and the other satellite's orientation was varied between -90 to $+90$ deg. These scenarios were run at 15 deg increments. Additional scenarios were run between -15 and $+15$ deg at 3 deg increments because small attitude changes were necessary during satellite operations. Figure 11 is a plot of the linear distance between the satellites as a function of time for a few of the scenarios run. The data were processed at 1 min increments, which was the highest fidelity of the plug-in. The results showed that the greatest change in orientation angle had the greatest separation distance over time. It should be noted that the change in distance could be very fast with the higher change in orientation, seeing a separation distance of 200 km in just four to six days.

To compute the acceleration rates, each scenario was plotted and fitted with a trendline. For each scenario, a second-order polynomial fit was nearly exactly matched. Figure 12 is a plot with the linear separation distance between the high-drag satellite and the second satellite in a pure low-drag orientation of $+90$ deg. With this scenario performed, a second-order polynomial curve was generated through linear least-squares regression. The second derivative of the calculated equation was used to find the acceleration. This was repeated for each scenario, and Fig. 13 is the relative acceleration rate that was computed for each change in orientation. Not included is the 0 deg change because this output showed no change in distance. The relative acceleration rates were found to have a greater effect as the difference in orientation angle was increased, with the rates between -15 and $+15$ deg having a very minimal change in acceleration rate. The maximum relative acceleration rates were at $+90$ and -90 deg, with rates of approximately 2.59×10^{-6} and 2.60×10^{-6} m/s^2, respectively.

IV. Case Study: RANGE Mission After Initial Satellite Separation

This case study evaluates a possible maneuver schedule for the RANGE satellites after they finished their detumble and initiated a small kickoff force to separate the two satellites. The starting orbit of preseparation but post-detumbling was set as a circular near-polar orbit with an altitude of 500 km. A kickoff force would impart an instantaneous velocity change of 1 cm/s on each satellite in opposite directions along the intrackvelocity direction. The orientation of the

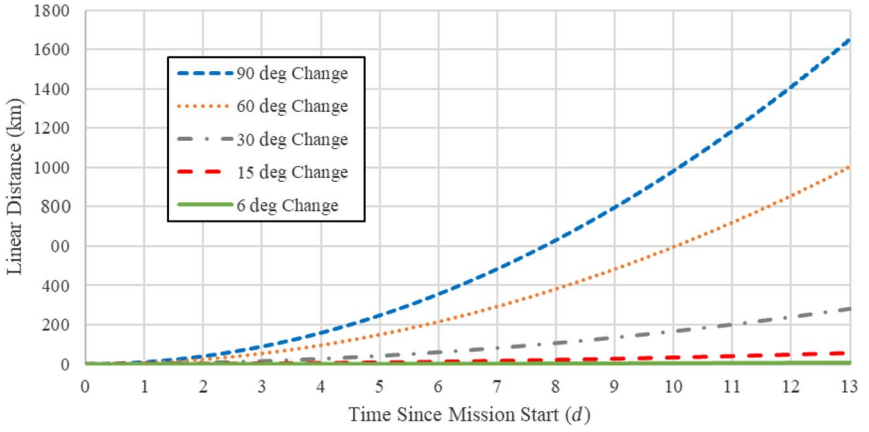

Fig. 11 Satellite separation with varying attitude differences.

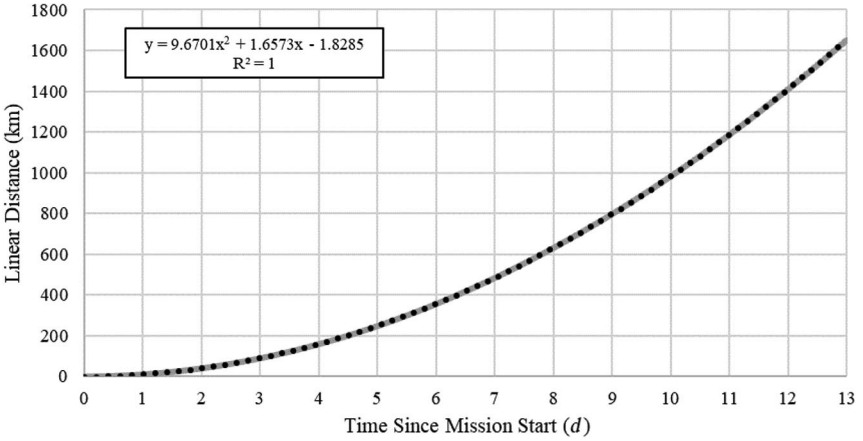

Fig. 12 Linear least-squares regression analysis of the distance between maximum high-drag- and low-drag-orientated satellites.

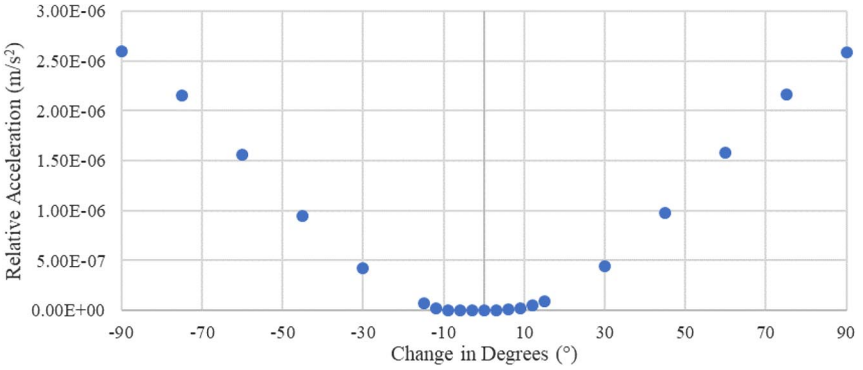

Fig. 13 Relative acceleration rates from the maximum high-drag orientation angle.

two satellites would be in the low-drag mode when the kickoff maneuver was initiated.

Although the kickoff force is small, it alters both orbits enough to create a difference in the orbital periods of 89.4 ms. With a periapsis velocity of 7.61 km/s, this results in an orbital drift that separates the satellites by 681 m per orbit. At that rate, it takes approximately 1.5 orbits for the two satellites to drift beyond 1 km. To counteract this separation, an initial maneuver will be performed. After a 5 min period to allow the satellites to reach a safe enough distance to begin maneuvers, the satellite with the longer period will change its orientation to the high-drag mode. The high-drag mode causes this satellite to drop in altitude faster than the other satellite, causing its orbit to speed up. The RANGE satellites have a set of orthogonal torque rods that provide three-axis control over the course of the orbit. In addition, each satellite has a single reaction wheel oriented such that the angular momentum vector of the wheel is in the crosstrack direction. This allows for quick and precise control of the pitch angle required for the differential drag maneuvers. Given this, the scenario only investigates pitch angle rotation for the satellites. This still allows for maximum and minimum reference areas normal to the spacecraft's velocity direction, enabling the greatest difference in drag potential.

A. First Maneuver: Counteracting Kickoff Force

Figure 14 shows the separation distance between the satellites after the first maneuver was performed. The final planned orientation of the satellites was in the high-drag mode, in which the antennas will be pointing at Earth. Because of this plan, the next step would be to match the orbital periods of the two satellites to stop the separation. When two satellites were in nearly circular orbits, if their orbital

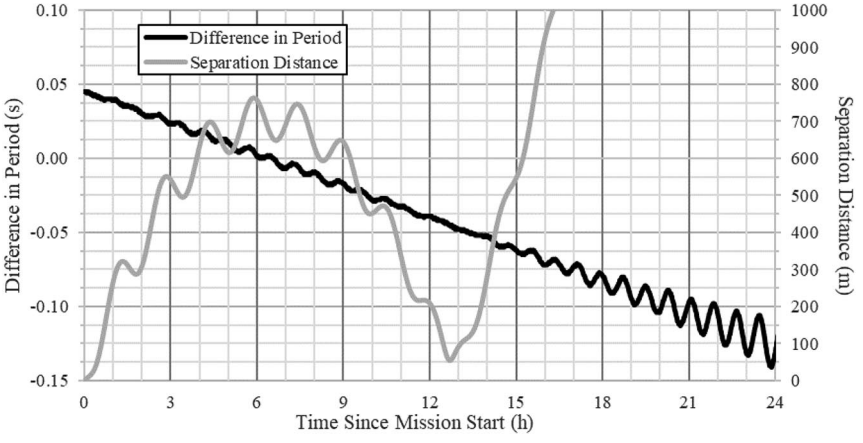

Fig. 14 Difference in orbital period and separation distance between satellites after the first maneuver.

periods were identical, they would both circle the Earth in the same amount of time, with both returning to their previous position. This meant that these two satellites would have no orbital drift causing an increase or decrease in separation distance between the satellites. Figure 14 also has the difference in the orbital period between the satellites and, from these data, the difference is relatively close to zero approximately 6 h after the kickoff separation. At this point, the second satellite (the satellite in the low-drag mode) slews until its orientation matches the high-drag satellite.

B. Second Maneuver: Removing Satellite Drift

After the second maneuver, the satellites achieve a stable, albeit oscillatory, separation distance, as observed in Fig. 15. Due to the kickoff maneuver and the fact that the drag forces do not impart instantaneous changes in velocity, the final difference in separation and period has some oscillatory behaviors. This is caused by an induced change to the eccentricity and the creation of a difference in the argument of perigee by 180 deg due to the kickoff force. Although the satellites have a near-circular orbit, these slight differences between satellites generate a pinwheel effect. With a very small kickoff force, the absolute minimum mean distance between the satellites after achieving stability is 707 m for this given scenario.

C. Third Maneuver: Bringing the Satellites Back Together

The next part of the planned maneuver was to reduce the satellites' distance to better facilitate the mission's objectives. To do this, the leading satellite entered a low-drag mode, causing the trailing satellite to accelerate toward the leading satellite. The challenge with this maneuver was that the trailing satellite would not only close the distance; it would drop in altitude to the point where, even when the satellite hit the desired distance, it would have a shorter orbital period and be moving at a greater relative velocity. The trailing satellite would therefore overtake the leading satellite, even if it was in the same orientation.

The solution to this problem is to have the trailing satellite perform an identical maneuver after a delay period. By mirroring the maneuver, the drop in altitude should be nearly identical for both satellites. There is, ultimately, a small difference in the drop in altitude because the leading satellite will return to high-drag mode at a higher altitude than the other satellite but, as long as the maneuver is for brief periods, the difference is negligible.

The maneuver is a two-step process for each satellite. The first step is to enter the low-drag orientation and to hold that mode for a set period. At the end of the desired period, the satellite returns to the high-drag orientation. After a set delay period, the second satellite follows the exact same process. This maneuver leads to two unknown values: the amount of time a satellite should be in the low-drag mode, and the length of time for the delay maneuver.

A key component to finding the unknown values was to calculate the separation acceleration rate between the satellites. To find this, the leading satellite was placed into a low-drag mode after the stabilized orbit was achieved. The maneuver was initiated when the difference in periods of the two satellites was close to zero during the oscillations.

To calculate the acceleration, a second plot was created for the period during this phase of the mission before the trailing satellite overtook the leading satellite. Figure 16 shows the linear distance between the satellites and a second-order trendline curve fit. From the plot, the acceleration between the satellites was -2.34×10^{-6} m/s^2. This value was within the same order of magnitude for satellites in a similar orientation, as discussed in Sec. III.B.

The next step was to compute the length of time for the satellite's maneuver t_M. A maneuver separation velocity V_M was obtained by integrating the acceleration a, and it was rewritten in terms of t_M to

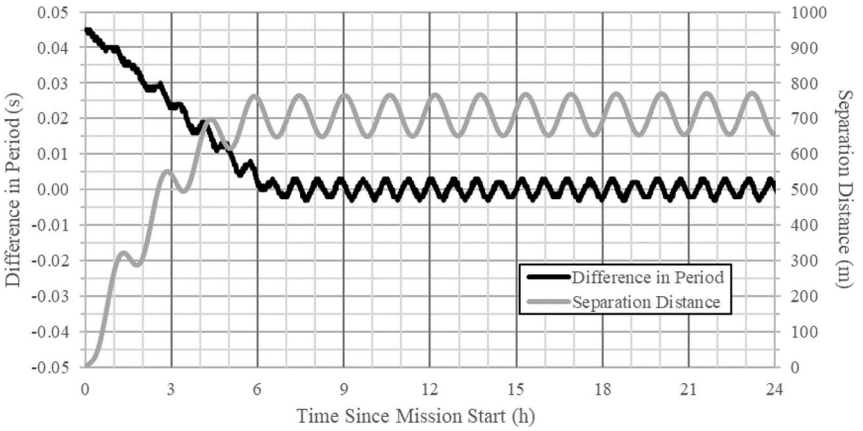

Fig. 15 Difference in orbital period and separation distance between satellites after the second maneuver.

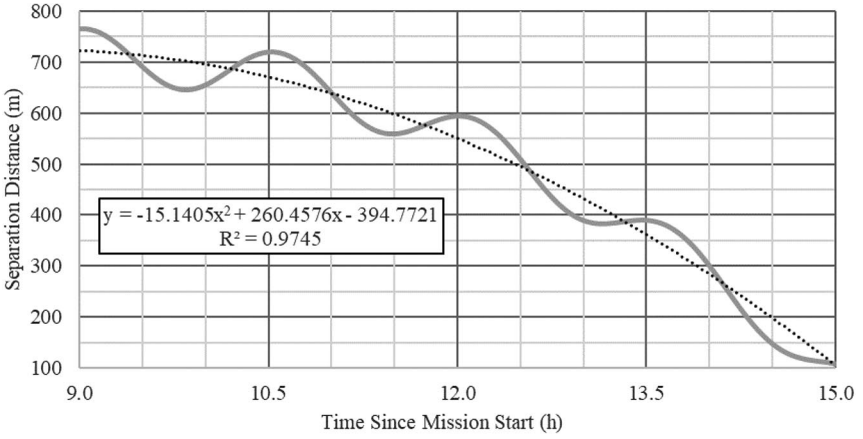

Fig. 16 Linear distance between satellites after the third maneuver and the second-order curve-fit trendline.

give Eq. (13), assuming the initial separation velocity was zero. V_M could be defined by the user and was chosen here to be 0.03 m/s, noting that different values would only impact the total maneuver time. From the acceleration that was already analyzed, t_M was computed to be approximately 225 min:

$$t_M = \frac{V_M}{a} \tag{13}$$

The other variable that needed to be calculated was the time to delay t_D. For this value, the desired change in distance d was also required. By rewriting Eq. (13), and given that distance was velocity multiplied by time, Eq. (14) was derived:

$$d = V_M t_D \Rightarrow t_D = \frac{d}{a t_M} \tag{14}$$

At this point, the satellites were a mean distance of 707 m, and a final distance of 75 m was desired. This meant that a change of distance of $d = 632$ m was needed, requiring a maneuver delay period that was calculated to be 334 min. When combining the delay period with the maneuver time period for the leading satellite, a total maneuver time period of 9.32 h was required. Figure 17 is a visual representation of this entire maneuver, and Fig. 18 is the linear distance between the two satellites for all the maneuvers, with special marking denoting when the final maneuvers were implemented. The numbers in Fig. 18 correspond to the maneuvers indicated in Fig. 17.

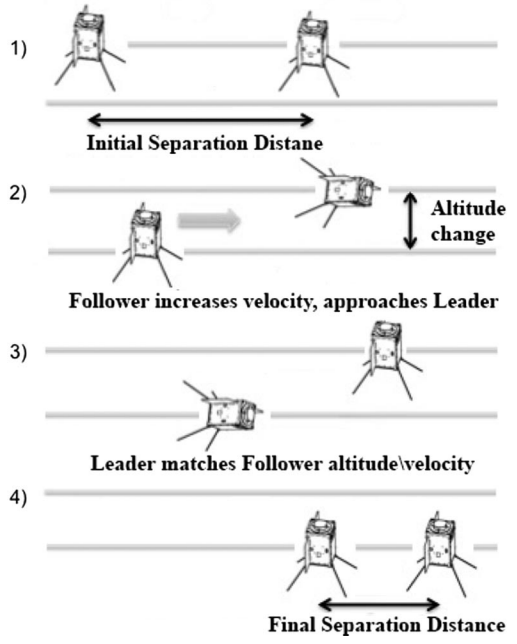

Fig. 17 Description of differential drag concept, adapted from the work of Gunter et al. [1].

D. Results

The outcome of this maneuver had the two satellites in a stable separation distance of about 75 m. The difference between the desired final distance and the theoretical using Eqs. (13) and (14) yielded a percent error of 0.0038%. Although this scenario validated the maneuver sequence, alterations would have to be made for the actual satellites that would launch. For the safety of the satellites, a larger mean final distance would be selected so that the satellites did not come so close during their lowest oscillatory distance. Additional measures, such as a smaller separation velocity and reducing the acceleration rate by not doing maximum differential drag orientations, could also be implemented. This would increase the safety measures for the satellites, should there be any complications, thus increasing the viability of the mission. The downside would be an increase in the time required for maneuvers to be completed.

V. Conclusions

The Ranging and Nanosatellite Guidance Experiment nanosatellites experience hyperthermal free molecular flow in orbit. A high-fidelity aerodynamic model for these satellites is developed using an industry-standard direct simulation Monte Carlo code: a direct simulation Monte Carlo analysis code. A sensitivity analysis in this regime indicates that the two primary variables are the accommodation coefficient and the orientation of the flowfield. Because the DSMC analysis code (DAC) cannot be directly integrated into orbit propagation software, a surrogate for the DAC is generated specifically for these satellites. This surrogate model applies numerical integration techniques developed in the meteorological community: using spherical geometry in the design of experiments and radial basis functions in the surrogate model. The radial basis function parameter is tuned to minimize the model error, which agrees to within 5% of the DAC validation runs.

Using a high-precision orbit propagator, a standard constant ballistic coefficient model is compared with the high-fidelity aerodynamic model. The results show that the difference in separation distance due to the aerodynamic model fidelity can exceed 800 m within 48 h. Using a rarefied flow model of the Ranging and Nanosatellite Guidance Experiment satellites, the initial separation dynamics are investigated. A series of maneuvers is developed that are designed to mitigate the initial kickoff velocity and stabilize the separation distance between the satellites. These results suggest that high-fidelity rarefied aerodynamics and high-precision orbit propagation allow for more

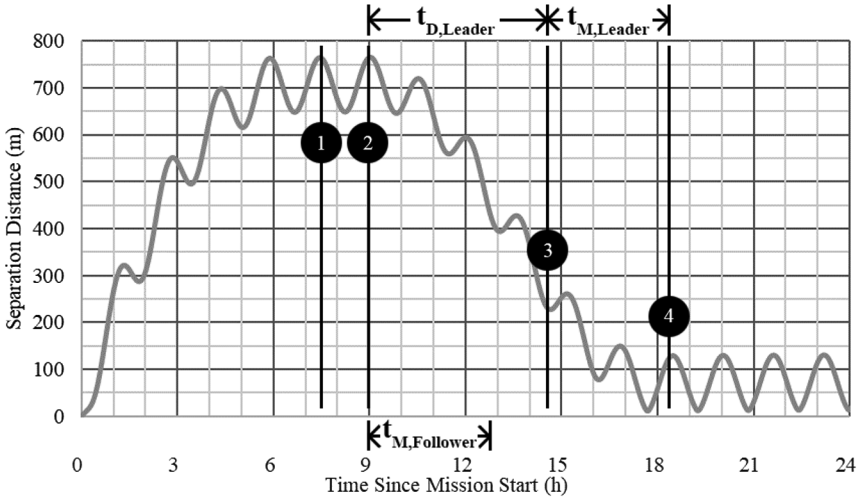

Fig. 18 Difference in the separation distance between the two satellites after the last maneuver.

accurate maneuver planning to control the relative position of satellites within a formation.

Acknowledgments

This research was supported in part by the U.S. Office of Naval Research under award number N00014-16-1-2167. This Note was presented as AAS Paper 17-753 at the 2017 AAS/AIAA Astrodynamics Specialist Conference.

References

[1] Gunter, B. C., Davis, B. T., Lightsey, G. E., and Braun, R. D., "The Ranging and Nanosatellite Guidance Experiment (RANGE)," *AIAA/USU Conference on Small Satellites*, Session V: Guidance and Control, Logan, UT, 2016, SSC16–WK–17, https://digitalcommons.usu.edu/smallsat/2016/S5GuidCont/3/.

[2] Leonard, C. L., Hollister, W. M., and Bergmann, E. V., "Orbital Formation Keeping with Differential Drag," *Journal of Guidance, Control, and Dynamics*, Vol. 12, No. 1, 1989, pp. 108–113. doi:10.2514/3.20374

[3] Horsley, M., "An Investigation into Using Differential Drag for Controlling a Formation of CubeSats," *Advanced Maui Optical and Space Surveillance Technologies Conference*, 2011, pp. E28, LLNL-CONF–498275, https://amostech.com/.

[4] Horsley, M., Nikolaev, S., and Pertica, A., "Small Satellite Rendezvous Using Differential Lift and Drag," *Journal of Guidance, Control, and Dynamics*, Vol. 36, No. 2, 2013, pp. 445–453. doi:10.2514/1.57327

[5] Gangestad, J., Hardy, B., and Hinkley, D., "Operations, Orbit Determination, and Formation Control of the Aerocube-4 CubeSats," *AIAA/USU Conference on Small Satellites*, Technical Session X: The Year in Review, 2013, SSC13-X–4, https://digitalcommons.usu.edu/smallsat/2013/all2013/116/.

[6] Omar, S. R., and Wersinger, J., "Satellite Formation Control Using Differential Drag," *53rd AIAA Aerospace Sciences Meeting*, AIAA Paper 2015-0002, 2015. doi:10.2514/6.2015-0002

[7] Pérez, D., and Bevilacqua, R., "Differential Drag-Based Reference Trajectories for Spacecraft Relative Maneuvering Using Density Forecast," *Journal of Spacecraft and Rockets*, Vol. 53, No. 1, 2016, pp. 1–9. doi:10.2514/1.A33545

[8] Mazal, L., Pérez, D., Bevilacqua, R., and Curti, F., "Spacecraft Rendezvous by Differential Drag Under Uncertainties," *Journal of Guidance, Control, and Dynamics*, Vol. 39, No. 8, 2016, pp. 1721–1733. doi:10.2514/1.G001785

[9] Boshuizen, C. R., Mason, J., Klupar, P., and Spanhake, S., "Results from the Planet Labs Flock Constellation," *28th Annual AIAA/USU Conference on Small Satellites*, Technical Session I: Private Endeavors, 2014, SSC14-I–1, https://digitalcommons.usu.edu/smallsat/2014/PrivEnd/1/.

[10] Foster, C., Hallam, H., and Mason, J., "Orbit Determination and Differential-Drag Control of Planet Labs CubeSat Constellations," *AAS/AIAA Astrodynamics Specialist Conference*, AAS Paper 15–524, Springfield, VA, 2015.

[11] Foster, C., Mason, J., Vittaldev, V., Leung, L., Beukelaers, V., Stepan, L., and Zimmerman, R., "Constellation Phasing with Differential Drag on Planet Labs Satellites," *Journal of Spacecraft and Rockets*, Vol. 55, No. 2, 2018, pp. 473–483. doi:10.2514/1.A33927

[12] Vallado, D., and McClain, W., *Fundamentals of Astrodynamics and Applications*, Space Technology Library, Springer, New York, 2001, pp. 551–574.

[13] Bird, G. A., *The DSMC Method*, CreateSpace, Scotts Valley, CA, 2013, pp. 13–32.

[14] Papitashvili, N., "NRLMSISE-00 Atmosphere Model" (online database), http://ccmc.gsfc.nasa.gov/modelweb/models/nrlmsise00.php [retrieved 11 Dec. 2015].

[15] Alexeenko, A., "Gas Dynamics Toolbox Applet," July 2009, https://web.ics.purdue.edu/~alexeenk/GDT/index.html [retrieved 11 Dec. 2015].

[16] Picone, J., Hedin, A., Drob, D. P., and Aikin, A., "NRLMSISE-00 Empirical Model of the Atmosphere: Statistical Comparisons and Scientific Issues," *Journal of Geophysical Research: Space Physics*, Vol. 107, No. A12, 2002, pp. SIA–SIA 15-16. doi:10.1029/2002JA009430

[17] Moe, K., and Moe, M. M., "Gas-Surface Interactions in Low-Earth Orbit," *International Symposium on Rarefied Gas Dynamics*, AIP Conference Proceedings, edited by D. A. Levin, I. J. Wysong, and A. L. Garcia, AIP Publ., Melville, NY, 2011, pp. 1313–1318. doi:10.1063/1.3562825

[18] Imbro, D. R., Moe, M. M., and Moe, K., "On Fundamental Problems in the Deduction of Atmospheric Densities from Satellite Drag," *Journal of Geophysical Research*, Vol. 80, No. 22, 1975, pp. 3077–3086. doi:10.1029/JA080i022p03077

[19] Harrison, I. K., and Swinerd, G. G., "A Free Molecule Aerodynamic Investigation Using Multiple Satellite Analysis," *Planetary and Space Science*, Vol. 44, No. 2, 1996, pp. 171–180. doi:10.1016/0032-0633(95)00077-1

[20] Schaaf, S. A., and Chambré, P. L., *Flow of Rarefied Gases*, Princeton Univ. Press, Princeton, NJ, 1961, pp. 2–18. doi:10.1002/aic.690080307

[21] Regan, F. J., and Anandakrishnan, S. M., *Dynamics of Atmospheric Re-Entry*, AIAA, Reston, VA, 1993, pp. 309–368, Chap. 11. doi:10.2514/4.861741

[22] Rader, D. J., Trott, W. M., Torczynski, J. R., Casteñeda, J. N., and Grasser, T. W., "Measurements of Thermal Accommodation Coefficients," Sandia National Labs. TR SAND2005-6084, Albuquerque, NM, Oct. 2005. doi:10.1116/1.4901011

[23] Maxwell, J. C., and Niven, W. D., *The Scientific Papers of James Clerk Maxwell*, Vol. 2, Dover, New York, 1890, pp. 26–78. doi:10.1017/CBO9780511710377

[24] LeBeau, G. J., and Lumpkin, F. E., III, "Application Highlights of the DSMC Analysis Code (DAC) Software for Simulating Rarefied Flows," *Computer Methods in Applied Mechanics and Engineering*, Vol. 191, Nos. 6–7, 2001, pp. 595–609. doi:10.1016/S0045-7825(01)00304-8

[25] Baumgardner, J. R., and Frederickson, P. O., "Icosahedral Discretization of the Two-Sphere," *SIAM Journal on Numerical Analysis*, Vol. 22, No. 6, 1985, pp. 1107–1115. doi:10.1137/0722066

[26] Carfora, M. F., "Interpolation on Spherical Geodesic Grids: A Comparative Study," *Journal of Computational and Applied Mathematics*, Vol. 210, Nos. 1–2, 2007, pp. 99–105. doi:10.1016/j.cam.2006.10.068

[27] Vanderplaats, G. N., "The Golden Section Algorithm,"*Multidiscipline Design Optimization*, Vanderplaats Research & Development, 2007, pp. 63–69.

[28] Hart, K. A., Simonis, K. R., Steinfeldt, B. A., and Braun, R. D., "Analytic Free-Molecular Aerodynamics for Rapid Propagation of Resident Space Objects," *Journal of Spacecraft and Rockets*, Vol. 55, No. 1, 2018, pp. 27–36. doi:10.2514/1.A33606

[29] Groesbeck, D., Gunter, B. C., and Hart, K. A., "Simulated Formation Control Maneuvers for the RANGE CubeSat Mission," *2017 AAS/AIAA Astrodynamics Specialist Conference*, AAS Paper 17-753, Springfield, VA, 2017, pp. 3073–3092.